Dynamic Modeling of Local Reaction Conditions in an Agitated Aerobic Fermenter

Marko Laakkonen, Pasi Moilanen, Ville Alopaeus, and Juhani Aittamaa
Laboratory of Chemical Engineering, Helsinki Univ. of Technology, Finland

DOI 10.1002/aic.10782
Published online February 9, 2006 in Wiley InterScience (www.interscience.wiley.com).

Computational Fluid Dynamics (CFD) can be used to investigate local reaction rates and gas-liquid mass transfer in agitated aerobic fermenters, but it is too slow for the simulation of a whole fermentation batch at present computational capabilities. This problem is addressed in the present work by developing a dynamic model with 42 subregions for a 0.64 m^3 pilot xanthan fermenter. The model considers local reaction and mass transfer rates in the fermenter and the change of liquid flow fields during the fermentation. Gas-liquid mass transfer fluxes are calculated based on the simplified solution of Maxwell-Stefan diffusion by assuming the mass transfer resistance in both the gas and the liquid side of the gas-liquid interface. Gas-liquid mass transfer areas are obtained from Population Balances (PB) for bubbles. The comparison of model predictions to the laboratory stirred tank experiments with aqueous xanthan shows the need of local bubble size distributions (BSD) for the description of complex gas-liquid hydrodynamics and mass transfer. The model predicts the effect of operating conditions on the temporal and spatial variation of BSDs, mass transfer coefficients, dissolved oxygen concentrations, and xanthan reaction rates in the fermenter. It can be used to investigate fermenter operating strategies. The model is also useful for the scale-up studies. © 2006 American Institute of Chemical Engineers *AIChE J,* 52: 1673–1689, 2006
Keywords: bubble phenomena, mass transfer, mixing, fermentation, xanthan

Introduction

Agitated aerobic fermenters are widely used in the biotechnology, food, and pharmaceutical industries. Agitation improves mixture homogeneity and enhances heat and mass transfer, improving the reactor performance. Gas-liquid mass transfer limitations, non-ideal mixing, and time-dependent physical properties make the design and scale-up of large aerobic fermenters problematic.[1,2] Computational Fluid Dynamic (CFD) tools are useful for the investigation of local hydrodynamics, reaction rates, and mass transfer, but they cannot be used to simulate a whole fermentation batch at present computational capabilities. The computation time becomes critical, especially when reaction kinetics, rigorous gas-liquid mass transfer, and population balances must be solved simultaneously. The use of multiblock (or "compartmental" or "zone") models is an alternative approach. Multiblock models have been applied in many studies for the investigation of local gas-liquid hydrodynamics in stirred tanks,[3-10] although in most studies the liquid flow field is assumed to be stationary. In some recent works, multiblock models have been integrated to the CFD programs.[11-14]

Xanthan gum is an extracellular polysaccharide, which has widespread commercial applications as a viscosity-enhancer and stabilizer in the food and pharmaceutical industries. Xanthan is produced typically in agitated gassed vessels.[15-17] It is generally agreed that poor bulk mixing and low oxygen transfer rates from gas to liquid are the bottlenecks of xanthan fermentation.[16,18,19] The deficiency of oxygen occurs most likely in the stagnant zones of the reactor. This causes inefficient use of reactor volume and may result in poor gum quality.[20] The broth viscosity changes dramatically during the fermentation. Ini-

Correspondence concerning this article should be addressed to M. Laakkonen at marko.laakkonen@tkk.fi.

tially, the broth is similar to water, while at the end it becomes highly viscous and shear-thinning with a yield stress. The changing physical properties alter the flow field, local reaction, and mass transfer conditions in the fermenter. The measurement of local conditions from an opaque, viscous fermentation broth is difficult. Physical reactor models that consider local gas-liquid hydrodynamics and reaction rates are, hence, valuable tools for the investigation of fermenters.

In the present work, local reaction rates and gas-liquid mass are investigated in a 0.64 m^3 pilot xanthan fermenter by using a dynamic multiblock model. The emphasis is put on the physical aspects of bioreactor modeling. Population balances for bubbles and a rigorous mass transfer model are validated against laboratory stirred tank experiments with aqueous xanthan solutions.

Experimental Procedures

Gas-liquid hydrodynamics and oxygen mass transfer were measured from aqueous xanthan (Keltrol BT) solutions in a 194 dm^3 laboratory stirred tank (H = T = 0.63 m). Various phenomena were investigated separately to minimize their interdependencies. The vessel was fully baffled and agitated by Rushton turbine (D_I/T = 1/3). The impeller was located at height H/3 from the bottom of vessel. Surface baffles were included to avoid surface aeration. Gas was injected to the bottom, below the impeller through a 0.16 m ring sparger, which includes 12 holes of diameter 2 mm. The investigated variables were xanthan concentration (0-2.7 wt%), gassing rate (Q = 0.1-0.9 vvm), and agitation speed (155-475 rpm, 0.1-3 W/kg(liquid), Re_I = 200-3.5·10^5). The measured quantities included liquid viscosity, overall gas holdup, local bubble size distribution, power consumption of mixing, and oxygen mass transfer. Gas holdup was measured from the change of liquid level. Viscosities were measured with a Brookfield LV-E viscometer. Gassed power consumption was measured from the angular momentum with a strain gauge.

The dynamic gassing-out method[21] was used to investigate oxygen transfer. A polarographic probe (LT Lutron, DO-5510) was used to measure dissolved oxygen concentration. The actual fermentation broth was mimicked by including 20 g/L lactose, 2.5 g/L KH_2PO_4, 2.5 g/L $(NH_4)_2SO_4$, 1.5 g/L $Na_2S_2O_3$, and 0.2 ml/L defoamer (Structol SB2121) to the xanthan solutions. The measured surface tension against air was 42 mN/m for this mixture.

Local bubble size distributions were investigated by digital photography from aqueous xanthan without lactose or electrolyte additives. Due to opaque dispersion, photographing was possible only near the wall. The photographs were taken at four heights between the bottom and the surface of dispersion. The BSDs were analyzed by identifying 500-1500 bubbles manually as ellipsoids. A challenge was to identify a statistically relevant sample of both small and large bubbles for the BSD. The identification was made in two parts. The smaller than 1 mm bubbles were identified from a 5 × 5 mm^2 area and the larger bubbles from a 100 × 150 mm^2 area of photograph. The identifications from the small and large area of photograph were then combined to a BSD by area weighting. Identifying bubbles from at least five photographs should minimize the transient effects. The particle analysis tool of ImageJ 1.32 freeware was used to convert the ellipsoids in thresholded images to the BSDs. The 6.5 Mpix resolution of the digital camera allowed the detection of larger than 0.1 mm diameter (~5 pixels) bubbles.

Xanthan Fermentation Kinetics

Unstructured kinetic models have been used most commonly to describe xanthan fermentation.[22] In these models, a microorganism is considered as an abstract thing called biomass, but often some essential nutrients, such as nitrogen source and oxygen, have been neglected.[23] The metabolically structured kinetic model of Garcia-Ochoa et al.[17,24] is used. The model considers the growth of biomass and the consumption of carbon source and oxygen while it is still rather simple. The oxygen consumption links the xanthan production rate to the gas-liquid mass transfer. The reaction rate equations are represented below in a simplified form by substituting the kinetic constants at the temperature 28°C.

Biomass (B) growth rate

$$r_B = 0.535 \cdot c_B(0.16466 \cdot c_{B0} + c_{N0})\left(1 - \frac{c_B}{c_{B0} + 6.073 \cdot c_{N0}}\right) \quad (1)$$

Xanthan gum (X) production rate

$$r_X = 6.0682 \cdot 10^4 \cdot c_{O2} \cdot c_B(7.1644 \cdot 10^{-3} + 1344 \cdot c_{O2}) \quad (2)$$

Carbon (S) source consumption rate

$$r_S = -1.1581 \cdot r_X - 985.95 \cdot c_{O2}c_B(0.9744 - 4811.6 \cdot c_{O2}) - 5.4945 \cdot r_B \quad (3)$$

Oxygen (O2) consumption rate

$$r_{O2} = -3.2496 \cdot 10^{-4} \cdot r_X - 32.865 \cdot c_{O2} \cdot c_B - 7.0413 \cdot 10^{-3} \cdot r_B \quad (4)$$

Nutrient (N) consumption rate

$$r_N = -0.16466 \cdot r_B \quad (5)$$

The production of carbon dioxide is included, because it reflects the cell respiration and is often monitored from the fermenter off-gas. In general, dissolved carbon dioxide may also influence the cell metabolism.[25] The production rate is taken to be equal to the oxygen consumption rate. The carbon mass balance analyses support this assumption.[16]

$$r_{CO2} = -r_{O2} \quad (6)$$

The kinetic model predicts that initial concentration of a nutrient limits the biomass growth. The xanthan production rate depends on the microbial and the dissolved oxygen concentrations. A pitfall of the kinetic model is that xanthan production can continue even after the carbon source has been consumed. Also, the consumption of oxygen can continue even

when dissolved oxygen is not available. These deficiencies are considered in the model implementation by enforcing the xanthan production and oxygen consumption rates to zero in the case when carbon source and dissolved oxygen have been consumed.

Water and nitrogen are included as non-reacting compounds to the investigated model system. Similarly, as oxygen and carbon dioxide, they are assumed to transfer between gas and liquid. It is noted that actual xanthan fermentation broths are much more complicated, including numerous organic compounds and salts.[22]

CFD Simulations

Eulerian gas-liquid CFD simulations (CFX 5.7) were made to obtain liquid flow fields in the laboratory stirred tank and pilot fermenter for the multiblock model. The pilot fermenter is a fully baffled vessel (T = 0.8 m, H = 1.6 m, liquid level at 1.3 m). It is agitated by three Rushton turbines (D_I = 0.25 m, D_I/T = 0.31). Gas is injected to the bottom of the vessel below the impeller through a 0.04 m diameter pipe.

Both laboratory vessel and fermenter were modeled as 180° segments with grids of 100,000 volume elements. Due to convergence problems, the gas feed pipe in the fermenter had to be modeled as a 2D-ring sparger. The SST turbulence model in the CFX-5.7 and the Multiple Reference of Frames (MRF) technique of impeller motion were used in the simulations. The shear-thinning behavior of aqueous xanthan was described by the model of Carreau[26]:

$$\frac{\mu_{eff} - \mu_\infty}{\mu_0 - \mu_\infty} = [1 + (\lambda\gamma)^2]^{(n-1)/2}, \tag{7}$$

where xanthan concentration dependent parameters are μ_∞ = 0.001, $\mu_0 = 0.001 + 93\cdot(c_X/wt\%)^{3.6}$, $n = 1.0\text{-}0.8\cdot(c_X/wt\%)^{0.11}$, $\lambda = 0.72 + 19\cdot(c_X/wt\%)^{3.1}$. They were adjusted against viscosity measurements covering 150 measurement points and the xanthan concentration range 0.1-2.7 wt%.

The effects of viscosity on the liquid flow field were investigated. The 194 dm^3 laboratory stirred tank was simulated at xanthan concentrations 0, 0.25, and 0.75 wt%, stirring speed 390 rpm, and gassing rate 0.5 vvm. The bubble sizes used were 2.5, 5, and 10 mm, respectively. The pilot fermenter was simulated at stirring speed 500 rpm and gassing rate 0.5 vvm at xanthan concentrations 0, 0.25, 0.75, 1.5, 2.0, and 2.5 wt%. The bubble sizes were 2.5, 5, 10, 13, 16, and 19 mm, respectively. Careful selection of bubble size was important because of the easy gas accumulation due to low rise velocities of bubbles in a highly viscous liquid. Due to the same reason, the swarm correction presented in our earlier study[27] was included. The CFD simulations showed that a fixed bubble size is not adequate for describing highly viscous gas-liquid flows. The predicted flow fields were used for the multiblock modeling because experimental information was not available.

Multiblock Stirred Tank Modeling

The laboratory and pilot vessel were divided into subregions based on the analysis of CFD simulation results. A heuristic approach was adopted because the development of automated algorithms[13,14] was outside the scope of the present work. The following criteria were applied for the compartmentalization:

- The subregions are arranged so that the main directions of liquid and gas flow can be described by a minimum number of subregions.
- Spatial inhomogeneity of a variable should be minimal inside a subregion.
- The gradient of a variable should remain nearly constant along the subregion interface.
- The model should be applicable for varying xanthan concentrations.

The created multiblock models for the laboratory stirred tank and pilot fermenter are presented in Figures 1a and 1b. The laboratory stirred tank model includes 21 subregions and is used for the submodel validation against the experiments. The pilot fermenter model includes 42 subregions.

The present modeling strategy was discussed in our earlier studies,[10,28] but is represented shortly to introduce some additional features for the fermenter modeling. The model consists of *NB* ideally mixed subregions for which dynamic gas and liquid molar balances (*2·NC·NB*) and discretized population balances (*NP·NB*) for bubbles are solved. Scalar component balances (*NS·NB*) are included to describe biomass, xanthan, carbon source, and nutrient, because these components cannot be modeled easily as conventional chemical species with well-defined physical properties.

Local dissipation rates of mixing energy, and liquid flow rates between the subregions are related to the gassed power consumption of mixing. Gray[29] has shown that for rotating turbine impellers liquid flow rates ($F^*_{ij} = F_{ij}/N\cdot D_I^3$) are proportional to the power number as

$$F^*_{ij,g} = F^*_{ij,u}\frac{N_{p,g}}{N_{p,u}}. \tag{8}$$

This relationship has been adopted in some later studies.[4,30] Local dissipation rates of mixing energy are scaled similarly. Other sources of local turbulence energy dissipation are the kinetic energy of gas injection and the decrease of hydrostatic pressure in the bubbles as they rise.

The change of liquid flow rates is related to the xanthan concentration by power law fitting:

$$F^*_{ij} = F^\circ_{ij}\exp(a_{ij}c_X + b_{ij}c_X^2), \tag{9}$$

where F°_{ij} is the flow from subregion i to j in water without xanthan. Parameters a_{ij} and b_{ij} are adjusted against CFD simulations at varying xanthan concentrations. The fitted volumetric flow rates are constrained so that the sum of inflows is equal to the sum of outflows for each subregion ($\Sigma F^*_{ij} = \Sigma F^*_{ji}$).

The fitted flow fields showed generally smaller than 10% relative errors at varying xanthan concentrations compared to the CFD predictions. An example of fermenter flow field is presented in Figure 1b. The model predicts the cavern formation, which is a well-known phenomenon in agitated shear-thinning fluids.[31] The liquid flow rates decrease in the middle between impellers and near the surface of dispersion at high xanthan concentration. At the bottom of the vessel, impeller discharge flow is directed towards the bottom of the vessel at low xanthan concentration but becomes radial at higher than 2

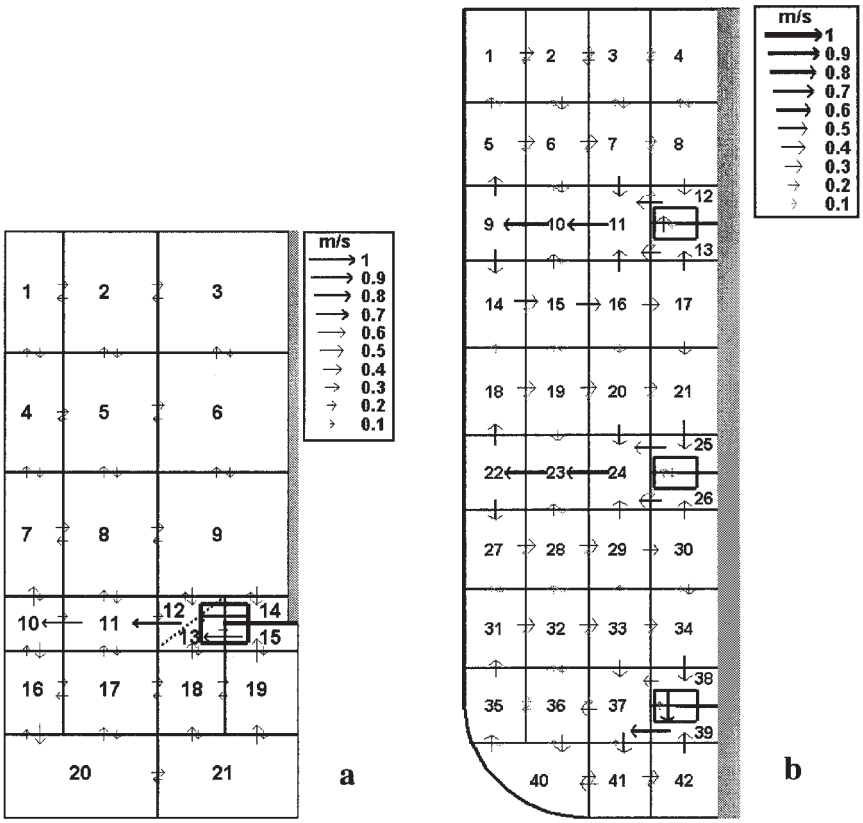

Figure 1. The division of (a) laboratory stirred tank and (b) 0.64 m^3 pilot fermenter into subregions with the predicted liquid flow field (c_x = 2 wt%, Q = 0.5 vvm, N = 500 rpm).

wt% xanthan concentration, being similar to the middle and top impellers.

Local turbulent energy dissipations and shear rates vary with the xanthan concentration and are fitted to the CFD results similarly as flow rates. Dissipation rates are scaled so that their volume integral is equal to the measured power consumption of mixing. Local shear rates are made dimensionless by scaling them with the stirring speed. The fitting predicts that local turbulence dissipations and shear rates decrease with the increasing xanthan concentration in the stagnant zones of the reactor close to the liquid surface, and in the horizontal middle planes between impellers. Dynamic pressure gradients at the interfaces between subregions can be positive or negative and are fitted by a linear relationship instead of the power law. They are scaled to the second power of stirring speed according to the Bernoulli's equation.

Bubble velocities consist of the transportation due to convection and slip:

$$U_k = \frac{F_{ij}}{A_{ij}} + U_{slip,k}, \tag{10}$$

where A_{ij} is the area over which liquid flows from subregion i to j. The flow rate is assumed to be bi-directional. The values of A_{ij} vary with the flow field and are described by power law fitting to the CFD results. The sum of A_{ij} and A_{ji} is constrained to the actual contact area between two subregions. The flow of bubbles due to slip is assumed to cause a backward pumping of liquid so that gas and liquid flow are two-way coupled. This also ensures that relative volumes of subregions do not change due to bubble slip.

The volumes of subregions are allowed to vary in the multiblock model. They are obtained from the molar volumes and material balances in a subregion. Molar volumes of gas and liquid are related to the known local mole fractions, temperature, and pressure according to the density correlation for liquid and the equation of state for gas. The relative volumes of subregions are forced to follow material balances and phase densities so that they remain unchanged. This necessitates an additional term to the impeller speed independent liquid flow rates. The excess volume in a subregion causes the increase of liquid flow rate as follows:

$$F^*_{ij} = F^*_{ij,0} + \frac{A_{ij}}{\sum_{j=1}^{NB} A_{ij}} \left(\frac{V_i}{V_{i,0}} - \frac{V_j}{V_{j,0}} \right) \cdot \frac{1}{\tau}, \tag{11}$$

where τ is a relaxation parameter that describes the residence time of extra volume in a subregion. This parameter is needed because momentum balances (i.e., the fluid flows) are not solved in the multiblock model. Eq. 11 is needed also because gas inlets and outlets from a subregion cause volume changes.

The model is solved by using the Gill's modification of the 4th order Runge-Kutta ODE-solver. The solver has an adaptive time step, which is adjusted based on the computation accuracy. Accuracy is tested comparing the result of single and

double increment of the time step. Numerical methods for stiff ODEs (VODE package in www.netlib.org) showed no improvement in the computation speed, thus indicating that the system of equations is not stiff. The solution of mass transfer fluxes and bubble slip velocities introduces non-linear algebraic equations to the model. They could be solved simultaneously with ordinary differential equations as a DAE system. Newton-Raphson iteration of mass transfer fluxes and slip velocities inside the reactor model is, however, preferred, because a good initial guess from previous time step ensures their convergence typically within just a few iterations. Due to slow dynamic change of the flow field, it is also possible to decrease the updating frequency for most quantities, which saves some computation time. Turbulent energy dissipations, shear rates, pressure gradients, internal flow rates, reaction rates, bubble slip, and breakage and coalescence rates are not updated at every time step. All values must then be saved to the workspace vector during these updates, but computation speed increases significantly without reducing the accuracy.

Population Balances for Bubbles

Bubble size is a key parameter for the description of gas-liquid hydrodynamics and mass transfer. The present experiments, as well as earlier studies,[32,33] have shown that assuming an average bubble size is a rough approximation in the stirred tanks and especially in highly viscous liquids. The modeling of bubble size distributions is, hence, preferred.

Population balance is a generalized approach for describing local bubble size distributions.[34-36] The BSDs are solved from discretized population balances for each subregion of the multiblock model:

$$\frac{dY_k}{dt} = \frac{U_k A_{ij} Y_k}{V_i} + \sum_{p=k+1}^{NP} \beta(d_k, d_p)\, g(d_p) Y_p \Delta d + \sum_{p=1}^{\#(V_p/2)} h((d_k^3 - d_p^3)^{1/3}, d_p) Y_k Y_p - g(d_k) Y_k - Y_k \sum_{p=1}^{\#(V_{NP}-V_k)} h(d_k, d_p) Y_p + \frac{\Delta(b(d_k) Y_k)}{\Delta d}. \quad (12)$$

The balance equation includes: (i) the convective/slip flow of bubbles in and out of the balance region, (ii) the birth of bubbles by breaking and coalescing, (iii) the death of bubbles by breaking and coalescing, and (iv) the growth of bubbles. Physical closure models for the breakage and coalescence rates and an appropriate bubble size discretization strategy are needed to close the population balance.

Bubble slip velocity

Relative velocities (slip) between bubbles and liquid are solved from the force balance on bubble motion:

$$(\rho_C - \rho_D)\, g \cdot v \cdot \hat{z} - \nabla p \cdot v = \frac{1}{2} A_h C_D \rho_C \bar{U}_{slip} |\bar{U}_{slip}|, \quad (13)$$

where buoyancy and dynamic pressure gradients act as driving forces, and drag is the resisting force of the bubble motion.

Fermentation broths include electrolytes and surface-active agents, which immobilize the bubble surface. Tzounakos et al.[37] investigated the effect of surfactants on the rise of gas bubbles in power-law non-Newtonian liquids and used the following correlation for the bubble drag:

$$C_D = \begin{cases} \frac{24}{\mathrm{Re}}(1 + 0.173 \cdot \mathrm{Re}^{0.657}), & \mathrm{Re} < 135 \\ 0.95, & \mathrm{Re} > 135 \end{cases}, \quad (14)$$

where the bubble Reynolds number is calculated by using the apparent liquid viscosity. The apparent viscosities are calculated from Eq. 7 based on the assumption that local shear rate is a sum of liquid and bubble induced shear:

$$\gamma = \gamma_L + \frac{U_{slip}}{d} E(d). \quad (15)$$

The liquid induced shear rate is included, in contrast to the work of Tzounakos et al.[37] where bubbles rise velocities were investigated in stagnant liquids. Bubble aspect ratio is estimated from[38]:

$$E(d) = \begin{cases} 1.1, & \mathrm{Re} \cdot Mo^{0.078} < 4 \\ 1.88 \cdot (\mathrm{Re} \cdot Mo^{0.078})^{-0.386}, & 4 \le \mathrm{Re} \cdot Mo^{0.078} \le 15, \\ 0.66, & 15 < \mathrm{Re} \cdot Mo^{0.078} \end{cases} \quad (16)$$

which was developed by fitting against the photographing experiments with shear-thinning CMC solutions. A characteristic feature of Eq. 16 is that small bubbles have a streamlined rear part that leads to the aspect ratio larger than one. Similar observation was made from aqueous xanthan solutions in the present work.

Bubble breakage

Bubble breakage depends on the balance between external stresses that disrupt the bubble and surface stresses that resist the bubble deformation.[39] A bubble breaks if the energy of a turbulent eddy is larger than the stabilizing surface tension force. Only eddies with length scales smaller than the bubble diameter can induce the breakage.

Luo and Svendsen[40] developed a widely used phenomenological model for bubble breakage based on the surface energetic aspects. It has been observed in many later studies[40-43] that this model depends on the size discretization. The deficiency has been corrected in some recent models by including capillary pressure constraints,[41-43] which, however, lead to mathematically complicated expressions. The model of Luo and Svendsen[40] is used here with a slight modification. The dependence on size discretization is avoided by integrating the breakage rates over all breakup volume fractions:

$$g(d_k) = C_1 \cdot (1-\phi)\left(\frac{\varepsilon}{d_k^2}\right)^{1/3} \int_0^1 \int_{\xi_{\min}}^1 \frac{(1+\xi)^2}{\xi^{11/3}} \times \exp\left(-\frac{6\cdot\sigma[f^{2/3}+(1-f)^{2/3}-1]}{\rho_C \varepsilon^{2/3} d_k^{5/3} \xi^{11/3}}\right) d\xi df, \quad (17)$$

where parameter C_1 is of magnitude 0.46 and $\xi_{\min}$ is the ratio of minimum eddy size and bubble size ($= \lambda_{\min}/d_j$). The minimum eddy size is related to the Kolmogorov's microscale by $\lambda_{\min} = 11.4\cdot((\mu_{\text{eff}}/\rho_C)^3/\varepsilon)^{1/4}$. The use of Eq. 17 requires daughter bubble size distribution ("breakage kernel"). The model of Lehr et al.[42] is used:

$$\beta(d_n, d_p) = \begin{cases} \dfrac{6}{\pi^{3/2} d_n^3} \dfrac{\exp(-9/4\cdot C_2[\ln(2^{2/5} d_n \varepsilon^{2/5}(\rho_C/\sigma)^{3/5})]^2)}{1+\text{erf}(3/2\cdot\ln[2^{1/15} d_p \varepsilon^{2/5}(\rho_C/\sigma)^{3/5}])}, & 0 \le d_n^3 \le \dfrac{d_p^3}{2} \\ \beta(d_p - d_n, d_p), & \dfrac{d_p^3}{2} \le d_n^3 \le d_p^3 \end{cases}. \quad (18)$$

It originates from the model of Luo and Svendsen[40] and assumes that the length scale of an eddy is larger than the diameter of the smaller bubble fragment, which results from the binary breakage. The model predicts that unequal breakage is preferred as the size of the parent bubble increases. This agrees with the pipe flow experiments of Hesketh et al.[44] An adjustable parameter C_2 is included to improve the agreement against measured local BSDs from aqueous xanthan.

Bubble coalescence

The coalescence is described by combining the frequency of bubble collisions and the efficiency of coalescence. Bubble collisions are described based on analogy to the kinetic gas theory. It is assumed that a moving bubble of size d_k sweeps a "collision tube" with a cross-sectional diameter of $d_k + d_p$. Turbulence is considered as the dominant driving force for collisions. The collision frequency is calculated from the model of Coulaloglou and Tavlarides[45] with a small algebraic correction (Alopaeus et al.[28]):

$$h(d_k, d_p) = C_3 \cdot \varepsilon^{1/3}(d_k + d_p)^2 (d_k^{2/3} + d_p^{2/3})^{1/2} \lambda(d_k, d_p), \quad (19)$$

where C_3 is of magnitude 0.88.[33,41]

Coalescence efficiency is described as a film drainage process between the collided bubbles. The coalescence is assumed to occur if collided bubbles remain in contact for sufficient time so that the liquid film between them drains out until a critical film thickness is reached. The mobility of the bubble surface plays a significant role in the film drainage and is affected by the presence of electrolytes and surface-active agents,[46] which are present in the fermentation broths. The model of Chesters[47] for bubbles in turbulent flow is adopted:

$$\lambda(a_k, a_p) = \exp\left(-C_4\sqrt{\frac{We}{2}}\right), \quad (20)$$

where C_4 is of magnitude unity. The comparison of Eq. 20 to some other efficiency models[33,48,49] showed that the predicted coalescence efficiencies are of the same magnitude as long as C_4 is being adjusted.

Bubble growth

The growth of bubbles due to mass transfer is described according to the first order upwind scheme for the bubble diameter by a sink term to the next larger or a source from the next smaller category as:

$$\frac{\Delta(b(d_k)Y_k)}{\Delta d} = \left.\frac{B_{k-1}Y_{k-1}}{v_k - v_{k-1}}\right|_{B_{k-1}>0} - \left.\frac{B_{k+1}Y_{k+1}}{v_{k+1} - v_k}\right|_{B_{k+1}<0} - \left.\frac{B_kY_k}{v_{k+1} - v_k}\right|_{B_k>0} + \left.\frac{B_kY_k}{v_k - v_{k-1}}\right|_{B_k<0}, \quad (21)$$

where the volumetric bubble growth rate is:

$$B_k = -A_k \sum_{m=1}^{NC} N_m \bar{V}_m \quad (22)$$

If mass is transferred into the last size category, it grows in number, but not in diameter. Similarly, if mass is transferred from the first category, bubble number decreases in that category.

Due to low gas solubilities, the growth has a small effect on BSDs elsewhere but near the gas feed, where dry gas becomes saturated with water.

Bubble size discretization

In the stirred tanks, number BSDs are skewed strongly towards small bubble size while a significant fraction of the gas volume is in the large bubbles.[32,50] The higher the number of size categories, the better is the accuracy of the solution with the expense of computing time. A denser discretization is used for the small bubbles than for the large bubbles because this produces a more accurate solution compared to the equally sized discretization when the same number of categories is used. The discretization is calculated from the formulas presented in our earlier study.[10]

The change of bubble size during the fermentation has to be considered in the discretization. The liquid viscosity is low and bubbles are generally smaller than 5 mm at the start of fermentation; while at the end, the liquid becomes highly viscous and some bubbles may be of the magnitude of the impeller diameter. The adaptive discretization minimizes the discretization error. The adaptivity is obtained by monitoring the gas volume fraction in the last bubble size category. If the gas fraction in the last category exceeds a predefined maximum value, the integrator is stopped and population balance is rediscretized by using a larger maximum bubble size. Similarly, if the gas fraction in the last category decreases below a predefined minimum value, rediscretization is made with a smaller maximum bubble size. The integration is continued after the rediscretization from the time when it was stopped. New bubble populations are obtained by linear interpolation from the old

ones so that local bubble number and gas volume are conserved. The adaptive discretization not only improves the accuracy of the solution, but also makes the computation faster.

Gas-Liquid Mass Transfer

Gas-liquid mass transfer fluxes are solved assuming two-film resistance and Maxwell-Stefan multicomponent diffusion with the Toor-Stewart-Prober linearization of constant physical properties in the diffusion path.[51] The overall flux and the mole fractions at the gas-liquid interface are iterated so that the fluxes are equal and the mole fractions sum to unity at both sides of the gas-liquid boundary. The approximate formulas of Alopaeus[52] for the fractional powers and high flux corrections of mass transfer coefficient matrixes are used to speed up the calculation. The molar compositions of bubbles and the mass transfer fluxes are assumed to be independent of the bubble size. These assumptions are made to avoid excessive computational cost. The estimates for gas and liquid side mass transfer coefficients are needed to solve the fluxes.

Mass transfer coefficients

Mass transfer coefficients depend on the surface mobility of a bubble. For the mobile bubble surfaces, liquid side mass transfer coefficients approach the penetration theory of Higbie.[53] For rigid bubbles, they approach the values predicted by the equation of Frössling[54] according to the laminar boundary layer theory. Surface mobility depends on the bubble size and the presence of electrolytes or surface-active agents, which make the bubble surface rigid. Kawase et al.[55] derived a correlation for the liquid film mass transfer coefficients in power-law fluids based on Higbie's penetration theory:

$$k_L = C_5 \sqrt{D_L} \left(\frac{\varepsilon \cdot \rho_C}{K} \right)^{1/(2(1+n))}. \tag{23}$$

The model assumes that the exposure time of the fluid element is equal to the average replacement time of the viscous sublayer at the bubble surface. The proportionality constant C_5 is of magnitude 0.3.[55] Garcia-Ochoa and Gomes[56] made the sensitivity analysis and comparison of Eq. 23 to available empirical k_La-correlations for fermentation broths and concluded that, in general, the agreement is good. Eq. 23 can be applied for Carreau fluids by assuming that $\mu_\infty \ll \mu_{\text{eff}}$, $\mu_\infty \ll \mu_0$, and $(\lambda\gamma)^2 \gg 1$ in Eq. 7. The flow indexes then become equal for the Carreau and power-law fluids. The consistency index becomes $K = \mu_0 \lambda^{n-1}$.

Gas side mass transfer coefficients are calculated from the rational approximation for the transient diffusion inside a fluid particle.[57] The bubble life times needed by the rational approximation are estimated from local bubble concentrations and death rates by breaking and coalescing. Mass transfer areas are calculated assuming oblate or prolate ellipsoids according to the aspect ratio correlation (Eq. 16).

Gas-liquid equilibrium

Gas-liquid equilibrium for oxygen, nitrogen, carbon dioxide, and water is calculated from Henry's model. Fermentation broths include organic compounds and electrolytes, which decrease the gas solubility ("salting-out effect"). According to Sechenov's relation, the contributions of dissolved compounds can be assumed to be log-additive at sufficiently low concentrations.[58]:

$$\log_{10}\left(\frac{He_{mix}}{He_{water}}\right) = \sum_{m=1}^{NC} (h_m + h_G(T))c_m + \sum_{m=1}^{NI} (h_m + h_G(T))c_m, \tag{24}$$

where gas specific, temperature dependent solubility parameters $h(T)$ follow a linear relationship:

$$h_G(T) = h_{G,0} + h_{G,T}(T - 298.15\ K) \tag{25}$$

The values of solubility parameters have been reported for most ions and many organic compounds.[58,59] Henry's constants for slightly soluble gases in pure water are calculated from the widely accepted correlations.[60] For water, Henry's constant is estimated to be equal to its vapor pressure.

Results and Discussion

Model validation against stirred tank experiments

Unaerated and Aerated Power Consumption. The measurements from the laboratory vessel showed that ungassed power consumption decreases with increasing xanthan concentration as

$$N_{p,u} = 5.6 - 1.1 \cdot (c_X/w - \%) \quad R^2 = 0.88, \tag{26}$$

which applies for the xanthan concentration range 0-2.5 wt%. Eq. 26 agrees with earlier observations, namely, that ungassed power numbers are lower in shear-thinning than in Newtonian liquids at transient flow regime (Re_I = 10-2000).[19,32,61,62] It is noted that the decrease of power numbers with increasing viscosity might result partly from the increasing fraction of stagnant bubbles in the solution.[63]

The gassed power consumption is related to the ungassed power. Cui et al.[64] developed the following correlation for the Rushton turbine impellers, which has been recommended in the review of Gogate et al.[2]:

$$\frac{P_g}{P_u} = \begin{cases} 1 - 9.9(QN^{0.25}/D_I^2), & QN^{0.25}/D_I^2 < 0.055 \\ 0.48 - 0.62(QN^{0.25}/D_I^2), & QN^{0.25}/D_I^2 > 0.055, \end{cases} \text{ in SI units} \tag{27}$$

The gassed power numbers from Eq. 27 with ungassed powers from Eq. 26 are compared to the present measurements in Figure 2. The comparison shows good agreement.

Bubble Size Distributions. Bubble size varied in a wide range from 0.1 mm up to ~100 mm in the laboratory stirred tank experiments. Typical photographs from 0.13, 0.25, and 0.5 wt% xanthan solutions are presented in Figure 3. The majority of bubbles were smaller than 0.5 mm, as can be concluded from the 3×3 mm^2 zoomed area in Figure 3. This was characteristic

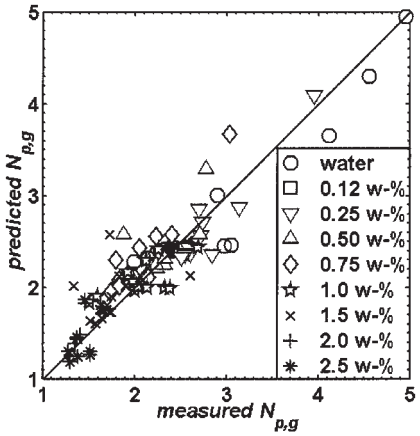

Figure 2. Predicted (Eqs. 26 and 27) vs. measured gassed power number of mixing at varying xanthan concentrations.

to all investigated solutions. Arithmetic mean bubble diameters d_{10} varied with the xanthan concentration, agitation speed, and gassing rate, being generally in the range 0.1-1.0 mm. The number of 2-5 mm bubbles decreased with increasing xanthan concentration, while the size of rare large bubbles increased (Figure 3). The observed Sauter mean bubble diameters were 1.9, 2.6, and 8.2 mm; and the maximum bubble diameters 10, 20, and 30 mm in the 0.13, 0.25, and 0.5 wt% solutions, respectively, just above the impeller plane (Figure 3). It seems that bubble size increased less near the wall than inside the dispersion. Bubbles of diameter 70-100 mm were observed to burst out from the surface of dispersion at larger than 1 wt% xanthan concentrations. The largest bubbles rose out in the middle and near the impeller shaft, thus indicating that gas was not completely dispersed.

Gas-liquid mixing is a complicated process, and a number of phenomena are involved. This makes the model validation a demanding problem. It is noted that creating similar turbulence conditions or investigating bubble slip, breakage, and coalescence separately is difficult even in a simpler flow apparatus. By making the experiments in a stirred tank, it can be ensured that all relevant phenomena are involved. In addition, this allows checking that model predictions are reasonable under varying agitation conditions. By incorporating population balances for bubbles to the multiblock model, it is possible to investigate local BSDs in a stirred tank. Unknown rate and proportionality parameters can be adjusted by comparing model predictions to the measured local BSDs. The effects of vessel geometry should be avoided in the adjustment because the scales, which are related to the physical phenomena, are much smaller than larger scales, which are related to the stirred tank. The larger scales are considered by dividing the vessel into subregions. Subregions have been selected so that the physical variables, such as turbulent energy dissipation and shear rate in the physical models, remain nearly constant inside a subregion. The resulting adjusted physical models should, hence, be applicable for an arbitrary reactor geometry.

The manual adjustment of parameters C_1-C_4 in Eqs. 17-20 was preferred because few BSDs were measured and good overall performance of the model was considered more important than obtaining a good fitting for some specific experiment. Even the manual adjustment produced fair agreement between the simulated and measured BSDs. The surface tension was set to 0.069 N/m in the coalescence efficiency model (Eq. 20). The number of bubble size categories was 100 in the simulation. The breakage rate parameter $C_1 = 0.46$ proposed by Luo and Svendsen[40] resulted in too small Sauter mean bubble diameters. A better agreement was obtained with $C_1 = 0.14$. A similar observation was made earlier with agitated air-water systems.[10] The analysis showed that arithmetic mean bubble diameters and number BSDs are sensitive to the daughter size distribution (Eq. 18). A reasonable prediction was obtained only by setting $C_2 = 0.3$ and assuming that $\beta(d_p - d_n,d_p) = \beta(d_n,d_p)$ for $d_n^3 \geq d_p^3/2$. This means that the daughter size distribution is skewed towards small bubbles and several small fragments are generated in a breakage event. The predicted BSDs seemed to be insensitive to the coalescence rate parameter C_3 in Eq. 19, which was set to 0.88 according to the theory of turbulent bubble collisions.[39] The predicted Sauter mean and maximum bubble diameters were sensitive to the parameter C_4 in the coalescence efficiency model (Eq. 20). A value lower than unity was needed to predict the presence of large bubbles

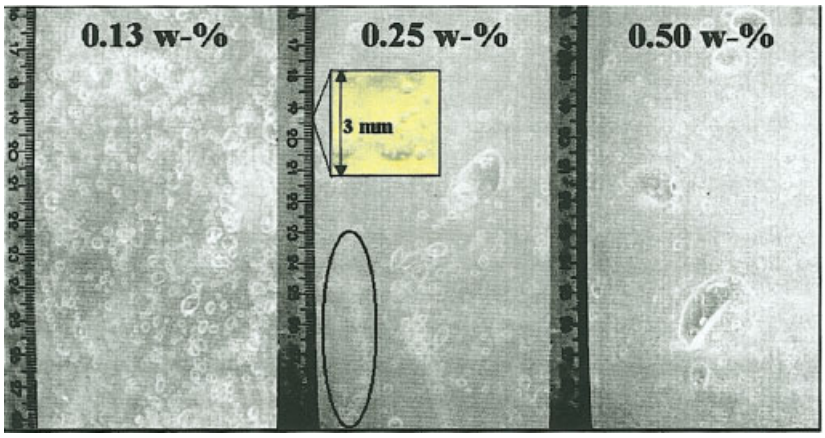

Figure 3. Effect of xanthan concentration on the bubble size above the impeller plane in the laboratory vessel (Q = 0.5 vvm, N = 390 rpm).

Scales in millimeters. [Color figure can be viewed in the online issue, which is available at www.interscience.wiley.com.]

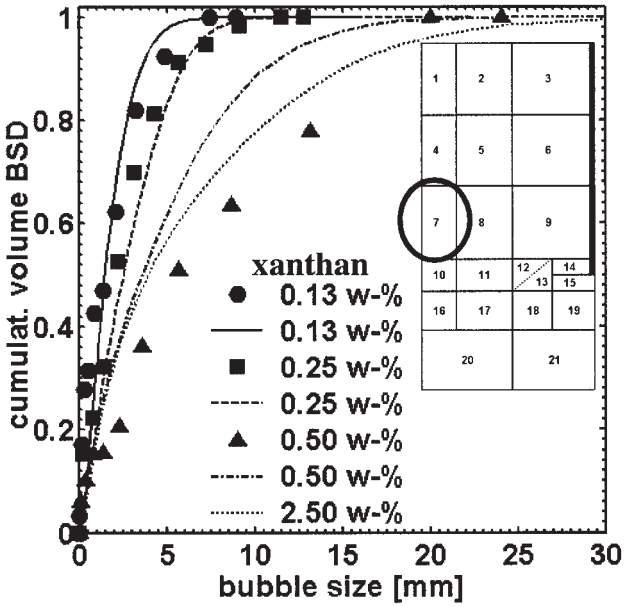

Figure 4. Measured (markers) and predicted (lines) cumulative volume BSDs above the impeller plane in the 194 dm^3 vessel (N = 390 rpm, Q = 0.5 vvm).

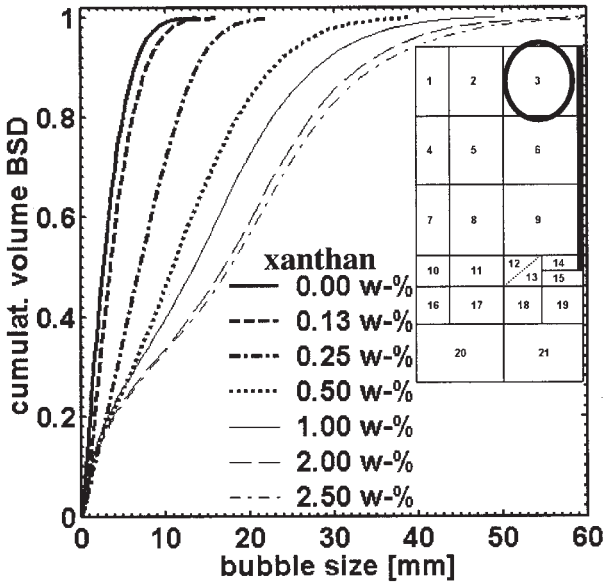

Figure 5. Predicted cumulative volume BSDs above the impeller plane in the 194 dm^3 vessel (N = 390 rpm, Q_g = 0.5 vvm).

(20-100 mm). The value $C_4 = 0.6$ seemed to be most satisfactory.

The measured and the simulated cumulative volume BSDs from 0.13, 0.25, and 0.5 wt% xanthan solutions are compared in Figure 4. The measurements are from the position just above the impeller plane, which corresponds to subregion 7 in the multiblock model for the laboratory vessel (Figure 1a). The agreement is good for the 0.13 and 0.25 wt% solutions. The deviation is larger for the 0.5 wt% solution. It is noted that bubble size varies in a wide range in a highly viscous solution (such as 0.5 wt%), thus making the reliable measurement of volume BSDs difficult.

Figure 5 presents simulated BSDs in the vicinity of the impeller shaft close to the liquid surface. The predicted maximum bubble sizes are ~60 mm at high xanthan concentrations. This agrees well with the observation of bubbles that rose out of dispersion. Even 40% of the gas volume is in bubbles of size larger than 20 mm at high xanthan concentrations. The fraction of stagnant bubbles of the total gas holdup increases from approximately 20% in the 0.5 wt% solution to 40% in the 2.5 wt% solution. Khare and Niranjan[32] have observed that stagnant bubbles may constitute 70-80% of the overall gas fraction in a stirred tank with CMC solutions, while Philip et al.[65] have reported 50% fractions for Newtonian liquids and much less for a shear-thinning liquid in an internal-loop reactor.

The measured and simulated local number and volume BSDs and mean bubble diameters in the 0.25 wt% solution are compared in Figures 6a and 6b. The agreement is good elsewhere but not in the topmost point near the surface. A significant spatial variation is predicted. The bubbles are smallest in the impeller region where turbulence intensities and breakage rates are high. Above the impeller, bubble size increases from the vessel wall towards the impeller shaft. This agrees with the observation that the largest bubbles rise in the middle and near the shaft. Bubble size increases from the impeller plane towards the surface. This becomes even more distinct at high xanthan concentrations. The decreasing breakage rates and the stagnant liquid layer near the surface of dispersion in a high viscosity liquid seem to explain this. Visual observations confirmed that rising bubbles stop at the edge of this layer and start to coalesce until the buoyancy becomes so large that they pass through it. Another interesting observation was that rising

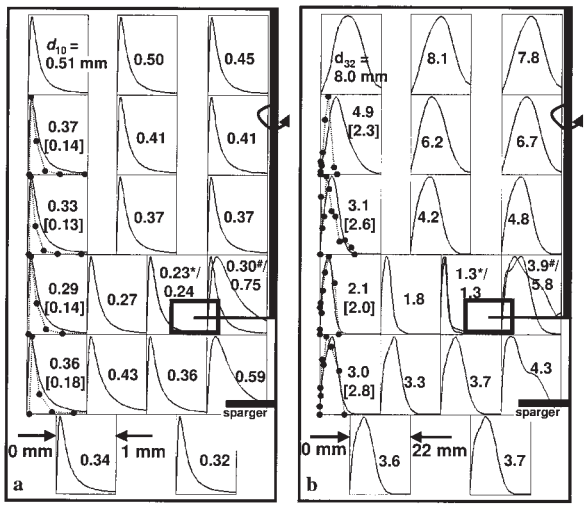

Figure 6. Measured (markers with dashed line) and predicted (solid lines) local (a) number BSDs (0-1 mm bubbles) and d_{10}, (b) volume BSDs (0-22 mm bubbles) and d_{32} in the 194 dm^3 stirred tank (0.25 wt% xanthan, N = 390 rpm, Q = 0.5 vvm).

* In front of/behind impeller blade, # above/below impeller.

bubbles tend to form trails. Such a trail is marked with an ellipsoid in Figure 3. The injection of bubbles to a stagnant xanthan solution showed that bubbles rise more rapidly in these trails than they would rise alone.

The adjusted breakage and coalescence models predict physically reasonable variation of BSDs with the xanthan concentration, stirring speed, and gassing rate. Care is, however, needed when the model is used for the scale-up, because the underlying physical mechanisms are not fully understood at the moment. Compared to the semi-empirical bubble size correlations, the prediction of local gas-liquid hydrodynamics, however, seems more realistic.

Gas Holdup. Overall gas holdup was investigated based on the change of liquid level. The measured gas holdups are "dynamic," including the gas that rises out within a few minutes after the agitation and gassing are stopped. Xanthan solutions were prepared by diluting a strong xanthan solution to a lower concentration. The smallest bubbles remained in the liquid after the dilution so that their fraction of the overall gas holdup could not be measured in all the experiments. Some accumulation of small bubbles occurred also during the preparation of the solution. Due to foaming and fluctuation of the liquid surface, the absolute errors of gas holdup are ± 1.5 vol%. The fluctuation was strong especially at high xanthan concentrations, when large bubble slugs burst out of the dispersion.

The time dependence of gas holdup, which is typical for high viscosity liquids,[32] was investigated in some experiments. Gas feed was started to a fresh solution, after which the liquid level was detected until it remained unchanged. Reaching a steady state required 5 minutes in a 0.25 wt% solution, 50 minutes in a 0.5 wt% solution, and 55 minutes in a 1.0 wt% solution. The fractions of stagnant bubbles of the overall gas holdup were 6.3, 28, and 36%, respectively. These are lower than Khare and Niranjan[32] observed in CMC solutions (70-80%). The simulation results in Figure 5 agree with the gas holdup measurements. The dependence of "dynamic" gas holdup on the xanthan concentration is rather weak. It seems that increasing bubble size compensates the lower bubble rise velocities due to high liquid viscosity. Experiments indicate that gas holdup decreases with increasing xanthan concentration at gassing rates higher than 0.5 vvm and increases at lower gassing rates. The decrease of impeller pumping capacity due to gassing apparently explains this.

Gas holdup should be predicted accurately to ensure accurate predictions of gas-liquid mass transfer. Measured and simulated gas holdups are compared in Figures 7a and 7b with xanthan concentration as a parameter. Overall, the agreement is satisfactory, although scatter in the measurements is large. Contrary to the experiments, a slight increase of gas holdup is predicted with the increasing xanthan concentration also at high gassing rates. The fact that the simulated gas holdups include small stagnant bubbles, which were excluded from most measurements, seems to explain the deviation. The predicted spatial distributions of gas holdup agree with the stirred tank experiments of Vlaev et al.[62] with 0.05-0.5 wt% xanthan solutions. The locus of maximum gas holdup shifts towards the impeller shaft with increasing xanthan concentration, while the regions near the wall become a trap for small bubbles. In the impeller region, gas holdup increases with liquid viscosity.

Oxygen Mass Transfer. Oxygen mass transfer was investigated in 0, 0.25, and 0.75 wt% xanthan solutions that mimicked the actual fermentation broth. The measurements with 0.75 wt% solutions proved to be most difficult, because poor mixing around the oxygen probe due to high liquid viscosity caused the increase of probe response time. For that reason, mass transfer was not measured at higher xanthan concentrations. A clear decrease of mass transfer rates was observed with increasing liquid viscosity.

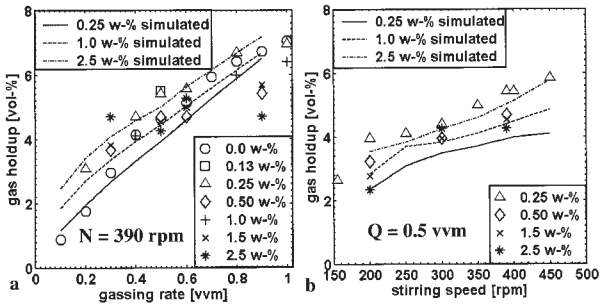

Figure 7. Predicted and measured gas holdups versus (a) stirring speed and (b) gassing rate in the 194 dm^3 stirred tank at varying xanthan concentrations.

The model predictions were validated by comparing to the measured concentration profiles of dissolved oxygen. The gas-liquid mass transfer area was obtained from population balances for bubbles. Although lactose or electrolyte additives were not used in the hydrodynamic and BSD experiments for which the PB model was validated, the dependence of bubble coalescence efficiency on the surface tension (Eq. 22) should consider the effect of additives on the bubble size. The measured surface tension 0.042 N/m for the aqueous mixture of additives and xanthan was used in the simulations.

It has been proposed in some studies that small bubbles are not active for the mass transfer, because they are in the equilibrium as a result of long residence time. In the present model, all bubbles were assumed to be active for the mass transfer. The analysis of Khare and Niranjan[32] supports this assumption. A reason for the active contribution of small bubbles could be the continuous breakage and coalescence of small bubbles, which causes the transfer of gas between small, stagnant bubbles and large bubbles.

The liquid side diffusion coefficients at infinite dilution were calculated from the correlation of Wilke and Chang[66] using the viscosity of water to avoid unreasonably low diffusion coefficients. The gas side diffusion coefficients at infinite dilution were calculated according to the Chapman-Enskog theory.[67] Gas-liquid equilibrium was obtained from Henry's model with salting-out correction.[58,59] The effect of xanthan macromolecules on the gas-liquid equilibrium was neglected. The predicted Henry's constants at 20°C are: water $1.34 \cdot 10^3$ Pa, oxygen $4.23 \cdot 10^9$ Pa, and nitrogen $8.34 \cdot 10^9$ Pa. The best agreement between the measurements and simulations was obtained with $C_5 = 0.3$ in Eq. 23. This value is the same as Kawase et al.[55] proposed for the agitated bioreactors.

Garcia-Ochoa et al.[17] developed the following correlation for actual xanthan fermentation broths:

$$k_L a = 6.14 \cdot 10^{-4} \cdot V_S^{0.5} \cdot \left(\frac{P_g}{V_T}\right)^{0.6} \cdot \mu_{eff}^{-0.5} \qquad (28)$$

Table 1. The Comparison of Measured and Predicted Oxygen Mass Transfer Coefficients

Xanthan [wt%]	Agitation Speed [rpm]	Gassing Rate [vvm]	k_La (1/s) (20°C)		
			Simulated	Measured	Garcia-Ochoa et al.[17]
0.00	225	0.15	0.012	0.013	0.028
0.00	225	0.27	0.017	0.018	0.034
0.25	225	0.15	0.0031	0.0050	0.0038
0.25	225	0.27	0.0051	0.0048	0.0047
0.25	275	0.27	0.0071	0.0072	0.0071
0.25	330	0.27	0.012	0.010	0.010
0.25	390	0.27	0.017	0.013	0.015
0.25	312	0.70	0.015	0.011	0.011
0.25	449	0.70	0.024	0.031	0.024
0.75	225	0.27	0.0012	0.0030	0.0017
0.75	225	0.52	0.0020	0.0034	0.0018
0.75	390	0.62	0.0051	0.0070	0.0062
0.75	449	0.70	0.0082	0.0052	0.0088
1.0	390	0.5	0.0040	—	0.0049
2.0	390	0.5	0.0028	—	0.0037
1.0	250	0.5	0.0013	—	0.0019
1.0	450	0.5	0.0063	—	0.0067
1.0	390	0.2	0.0037	—	0.0043
1.0	390	0.9	0.0055	—	0.0063

which is based on the dissolved oxygen experiments with dynamic technique in a 1.5 dm^3 fermenter. The authors state that the correlation covers a wide range of xanthan concentrations, but the actual range was not reported. The gassed power consumption in Eq. 28 was calculated from Eqs. 26 and 27. The effective viscosity was obtained from Eq. 7 by using the well-known relation $\gamma = 11.5 \cdot N$ for the shear rate.[68]

Model predictions are compared to the measurements from the laboratory vessel and the correlation of Garcia-Ochoa et al.[17] in Table 1. The simulated mass transfer coefficients k_La have been obtained following the same procedure that was applied to the measurements to allow the comparison.[21] Mass transfer coefficients were normalized to 20°C according to[69]:

$$k_La_{20} = \frac{k_La}{1.022^{(\theta-20)}} \tag{29}$$

Despite some deviation, the predicted mass transfer coefficients are in the same range with the measurements and the correlation (Table 1). In view of the complexity of the investigated system, the agreement is satisfactory, indicating that predicted mass transfer areas and coefficients are realistic. The deviations cannot be attributed to any specific error source.

Fermenter simulations

Initial Conditions and the Setup of the Simulation. The multiblock model for the 0.64 m^3 pilot fermenter together with population balances for bubbles, the gas-liquid mass transfer model, and the xanthan fermentation kinetics of Garcia-Ochoa et al.[17] were used to investigate the dynamics of xanthan fermentation. Water, carbon dioxide, oxygen, and nitrogen were included as chemical compounds in gas and liquid. Biomass (B), xanthan (X), carbon source (S), and nitrogen (N) were scalar components in liquid. The BSDs were described by 40 bubble size categories. More size categories would slightly improve the accuracy, but this is not critical in view of other measurement or modeling uncertainties. It is also noted that computation times largely depend on the number of size categories.

Cui et al.[64] investigated the power consumption in multiple impeller agitated vessels. Their results showed that the bottom impeller follows Eq. 27, while the following relation is more suitable for the middle and top impellers:

$$\frac{P_g}{P_u} = \begin{cases} 1 - 37.6 \cdot Q_{ij}N, & Q_{ij}N < 0.013 \\ 0.625 - 8 \cdot Q_{ij}N, & Q_{ij}N > 0.013 \end{cases} \tag{30}$$

where Q_{ij} is the local gas flow rate to the impeller. In the multiblock model, Q_{ij} is the local gas flow rate from subregion 30 to 26 and from subregion 17 to 13 for the middle and top impellers, respectively (Figure 1b).

Xanthan fermenters are operated typically by increasing the stirring speed towards the end of fermentation.[16,17] The aim is to ensure high xanthan reaction rates by minimizing the cavern formation and maintaining the high levels of dissolved oxygen (DO). Mixing and DO effects were investigated in two simulation cases, named S1 and S2. In S1, stirring speed was kept constant at 300 rpm during the fermentation batch. In S2, it was increased gradually from 300 to 475 rpm to maintain the mixture homogeneity and to ensure good mass transfer. Gas feed rate was 0.4 vvm in both simulation cases.

Initial concentrations were selected based on experimental xanthan fermentation studies.[17,18,24] The initial concentrations were for the carbon source 40 gC/L, biomass 0.06 gB/L, nutrient 0.5 gN/L, and xanthan 0 gX/L. The dissolved gases were assumed to be initially in equilibrium with the gas feed (78.07% N_2, 20.95% O_2, 0.94% H_2O, and 0.04% CO_2). The initial gas holdup and bubble size had no influence on the results, because they rapidly reached a pseudo steady state at the start of the simulation. The fermenter was assumed to operate at the known optimal temperature of 28°C.[17] Henry's constants were estimated for the mixture, which includes the major compounds of the optimized fermentation media (40 g/L glucose, 2.1 g/L citric acid, 2.9 g/L KH_2PO_4, 0.5 g/L $MgCl_2$,

0.1 g/L Na_2SO_4, 0.5 g/L NH_4NO_3, 0.2 g/L HCL).[17] The change of Henry's law constants during the fermentation was neglected. Henry's constants are at 28°C for H_2O $2.78 \cdot 10^3$ Pa, N_2 $9.63 \cdot 10^9$ Pa, O_2 $4.99 \cdot 10^9$ Pa, and CO_2 $1.91 \cdot 10^8$ Pa. The surface tension was set to 0.042 N/m.

Simulation was continued until xanthan concentration was 2.5 wt% in the fermenter. This corresponds to typical final concentration (1.5-3 wt%) in conventional fermenters.[16] In case S1, the final concentration was reached within 70 hours, while only 29 hours were needed in case S2. The simulation of a 70-hour batch took approximately 4 days wall-clock time with appropriate tolerances of integration. Long computation times are caused mainly by the short integration time step. This seems to be caused by the strong skewing of BSDs. Few large bubbles constitute a significant fraction of the gas volume, but their breakage rates are high, which necessitates short time steps. Another reason for short time steps seems to be the strong coupling of variables, i.e., that system of equations is not sparse. The updating of physical properties, breakage and coalescence rates, slip velocities, mass-transfer fluxes and flow fields also takes CPU time, although it is not done at every time step.

Overall Performance of Fermenter. The predicted overall gas holdup was 8.6 vol% at the start of fermentation. During the first 4 hours of fermentation, gas holdup first increased to 11 vol% and started to decrease when xanthan concentration reached 0.2 wt%. In case S1 gas holdup decreased to 5.8 vol%, and in case S2 to 6.0 vol% at the end. Machon et al.[70] have observed a similar turning point behavior of gas holdup with increasing pseudoplasticity. The initial rise of gas holdup seems to be caused by the accumulation of small gas bubbles; while the generation of large bubbles, which have short residence times, explains the decrease of gas holdup towards the end of fermentation.

The volume-averaged apparent viscosities of liquid increased to 1.3 Pa·s (S1, 300 rpm) and 1 Pa·s (S2, 475 rpm) in the 2.5 wt% xanthan at the end of the simulation. These viscosities are not comparable to those obtained from the approach of Metzner and Otto,[68] which neglects the variation of shear rates in the vessel. Local apparent viscosities varied from 0.4 Pa·s close to the impeller up to 1.8 Pa·s in the quiescent regions like at the bottom and near the surface. Vessel-averaged Sauter mean bubble diameters increased rapidly from 1.9 mm to 10 mm during the period 4-10 hours from the start-up, reaching 14 mm at the end of S1. The higher stirring speeds in case S2 favored the bubble breakage, resulting in smaller bubbles (~8 mm) at the end of S2.

Some trends of vessel-averaged quantities during S1 and S2 are presented in Figure 8. During the first 4 hours of fermentation, dissolved oxygen saturation is 100% (DO). After this, DO decreases rapidly below 30% of the saturation. In case S2, DO decreases more slowly due to gradual increase of stirring speed from 300 rpm to 475. This can be seen as jumps in the DO profile of S2. At constant stirring speed (S1), DO decreases monotonically. The main reason is the increase of liquid viscosity, which causes the increase of bubble size and decrease of gas holdup so that the specific gas-liquid mass transfer area decreases from approximately 280 to 25 m^2/m^3(dispersion) in S1 and 50 m^2/m^3(dispersion) in S2. The simulated DO profiles agree qualitatively with the pilot scale experiments of Amanullah et al.[16]

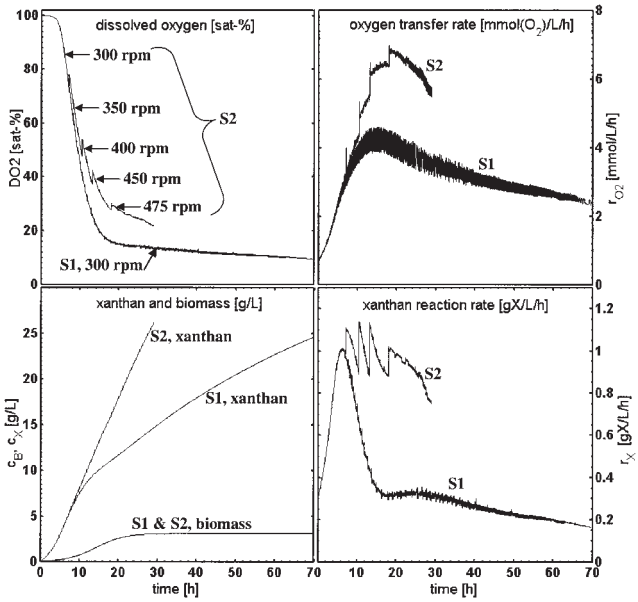

Figure 8. Overall performance of xanthan fermenter in simulation cases S1 and S2.

Oxygen transfer rates (OTR) (Figure 8) depend on the mass transfer coefficient, mass transfer area, and driving force, i.e., the departure from the equilibrium. The OTR is small at the start of fermentation because microbial concentration and oxygen consumption are small, but it increases rapidly, reaching a maximum (4-7 mmol/L/h), and decreases then slowly towards the end. The experiments of Garcia-Ochoa et al.[17] showed a similar trend. The decline of OTR results from the mass transfer limitation, which decreases DO, resulting in smaller biomass growth and xanthan production rates. The OTR starts to fluctuate when the broth becomes viscous. The frequency of fluctuation deviates from the updating frequency of flow fields and physical properties and seems to be caused by the numerical behavior of the model.

The comparison of S1 and S2 in Figure 8 shows the positive effect of stirring speed on the fermentation. The productivity of xanthan in S1 is 0.35 gX/L/h and much smaller than 0.88 gX/L/h in batch S2. The maximum biomass concentration is reached within 25 hours. The present model does not take into account the effect of cell damage on the biomass growth or xanthan production rate under high shear conditions such as in S2. It is noted that cells may become less sensitive to shear at high viscosities due to the protective viscous layer around them.[71]

The carbon dioxide concentration is measured typically from the fermenter off-gas, because it reflects the cell respiration.[18] The predicted dissolved carbon dioxide (DCO) showed similar but opposite trends compared to the DO. During the first few hours, DCO was 100% of the saturation, indicating that there was no mass transfer limitation. After this, DCO increased slowly to 170% of the saturation in S1 and to 150% of the saturation in S2 towards the end of the simulation, thus indicating that a mass transfer limitation exists for carbon dioxide as well.

From the process operation point of view, it is interesting to know how rapidly DO goes to zero, when gas feed is stopped. This may be helpful for evaluating the consequences of a process malfunction. The sensitivity of DO was investigated by

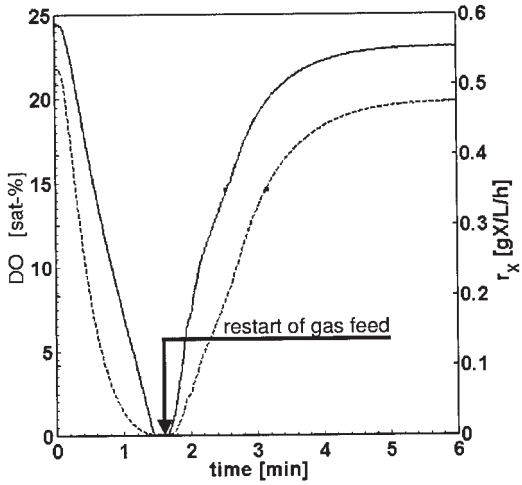

Figure 9. Effect of gas feed turn-off on the vessel-averaged dissolved oxygen concentration (solid line) and the xanthan reaction rate (dashed line) in the 0.64 m^3 fermenter (c_X = 1.1 wt%, N = 350 rpm, Q = 0.4 vvm).

stopping the gas feed for a moment, when xanthan concentration was 1.1 wt% and Oxygen Uptake Rate (OUR) 5 mmol/L/h. The simulated DO and xanthan reaction rate profiles are presented in Figure 9. Within one minute, the oxygen concentration decreases below the critical oxygen level of 10 sat%.[18] All oxygen is consumed within 1.5 minutes. After the restart of the gas feed, the DO and the xanthan reaction rate recover more slowly compared to the decline period. The simulation shows the sensitivity of xanthan fermentation to the gas feed.

Local Mass Transfer and Reaction Conditions. Earlier studies have shown that poor mixing results in inhomogeneous reaction conditions in xanthan fermenters.[12,16,19] The present simulations allowed investigating mixture inhomogeneities during the fermentation batch. The inhomogeneity can be evaluated based on the relative standard deviation of an interesting quantity s from:

$$SD = \frac{1}{\bar{s}} \sqrt{\frac{\sum_{i=1}^{NB} (s_i - \bar{s})^2}{NB}} \tag{31}$$

Another statistical parameter that characterizes the inhomogeneity is the spatial autocorrelation defined according to Geary's ratio:

$$GR = \left(\frac{NB - 1}{2 \sum_{i=1}^{NB} \sum_{j=1}^{NB} c_{ij}} \right) \left(\frac{\sum_{i=1}^{NB} \sum_{j=1}^{NB} c_{ij} (s_i - s_j)^2}{\sum_{i=1}^{NB} (s_i - \bar{s})^2} \right) \tag{32}$$

where c_{ij} is the binary connectivity matrix of multiblock model subregions. Element c_{ij} is unity if there is a connection between i and j and zero otherwise. The variation of an interesting quantity is smooth when GR is near to zero, while spatial gradients increase with increasing values of GR.

The SD and GR were calculated for the xanthan reaction rate and are presented in Figures 10a and 10b. The mixture is more homogeneous at large (S2) than at low (S1) stirring speed. This shows that the model predicts the effect of stirring speed on the

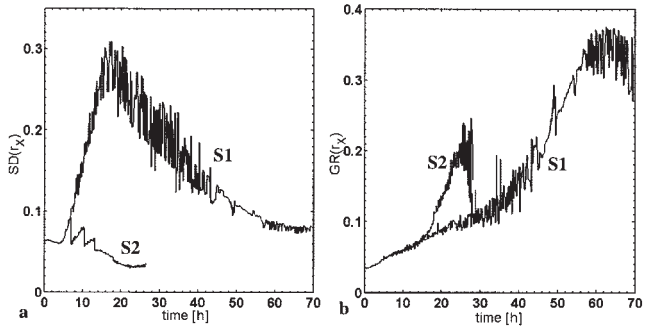

Figure 10. Spatial (a) standard deviation and (b) autocorrelation (Geary's ratio) of xanthan reaction rate in the 0.64 m^3 pilot fermenter.

mixture inhomogeneity. In S1, the standard deviation reaches a maximum during the period 10-20 h, when reaction rate is largest (Figure 8). The maximum of SD results from the gas-liquid mass transfer limitation. Reaction rates are largest at the bottom of the reactor near the gas injection point and in the impeller regions where oxygen transfer is most effective. The values of GR show that spatial gradients increase in the reactor towards the end of fermentation.

The spatial distribution of mass transfer and reaction conditions was investigated by taking some "snapshots" from different stages of fermentation. The first "snapshot" is from S1 at the time 20 h, when xanthan concentration is 1.2 wt% and the standard deviation of reaction rate is large (Figure 10a). The second "snapshot" is from S1 at the end of fermentation (t = 65 h, c_X = 2.4 wt%), when local spatial gradients are significant (Figure 10b). The last "snapshot" is at the end of S2 (t = 24 h, c_X = 2.2 wt%) at stirring speed N = 475 rpm (ε = ~4 W/kg).

Figure 11 shows the strong inhomogeneity of bubble sizes in the reactor. Bubbles are generally smallest in the impeller region and in the impeller discharge stream, i.e., between the impeller tip and the vessel wall. The largest bubbles exist in the

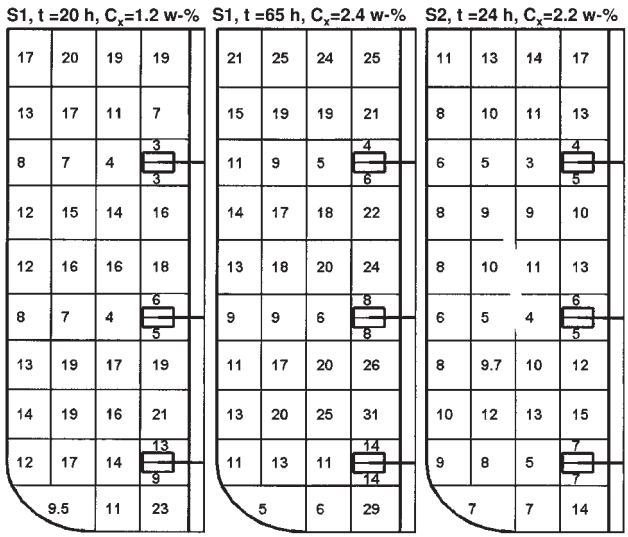

Figure 11. Predicted distribution of Sauter mean bubble diameters (d_{32}, mm) in the 0.64 m^3 fermenter.

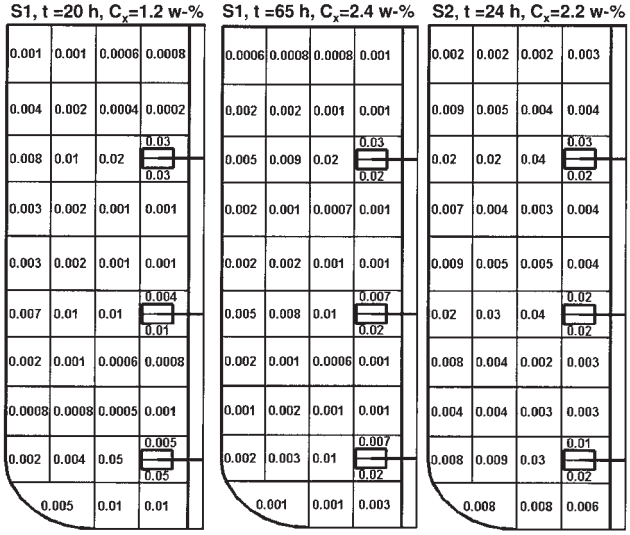

Figure 12. Predicted distribution of oxygen transfer coefficients (k_La, s^{-1}) in the 0.64 m^3 fermenter.

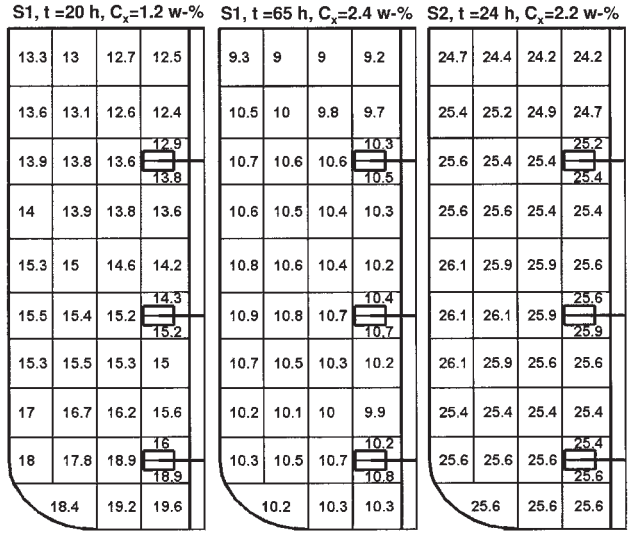

Figure 13. Predicted distribution of dissolved oxygen concentrations (DO, sat%) as a percentage of the saturation in the 0.64 m^3 fermenter.

middle between impellers and in the vicinity of the liquid surface, where apparent liquid viscosities are high. This indicates that bubbles must coalesce before they can rise through the stagnant layer of highly viscous liquid. High gas fractions favor bubble coalescence, resulting in large bubbles below the bottom impeller where gas is injected. Low apparent viscosities and high breakage rates explain the smaller bubbles in S2 than in S1 at the end of fermentation. An exception is the bottom of the reactor, where large bubbles are not transported at low stirring speed (S1).

The spatial distribution of volumetric oxygen transfer coefficients is presented in Figure 12. Local mass transfer coefficients are calculated from:

$$k_La = \frac{N_{O2}a_L}{c_{L,t}(x_{I,O2} - x_{B,O2})} \tag{33}$$

Figure 12 shows that mass transfer coefficients are largest in the impeller region and in the impeller discharge flow where the gas-liquid interfacial area and turbulence intensity are largest. Oxygen transfer coefficients are smallest in the regions where apparent viscosity and bubble size are largest, i.e., at the bottom, in the middle, and near the shaft between the impellers, and near the surface of dispersion, as expected. Mass transfer coefficients are larger in S2 than in S1 at the end of fermentation. Statistical analysis indicates that OTR is more homogeneous in S2 (SD = 0.97, t = 24 h) than in S1 (SD = 1.3, t = 65 h).

Local values of DO in Figure 13 are defined as a percentage of the saturated concentration at pressure 1.013 bar, temperature 28°C, and oxygen mole fraction 0.2095 in the gas. The DO decreases from the bottom towards the surface of dispersion in all simulations. This is caused mainly by the decrease of oxygen partial pressure from the bottom towards the surface. It is noted that local DO depends complicatedly on the mass transfer coefficient, reaction rate, flow field, and driving force for mass transfer. Axial variations are evolved, especially in case S1. Due to low liquid flow rates, DO is not convected efficiently to the top of the fermenter. In case S2, high liquid flow rates result in more homogeneous DO. The spatial variation of DO is smaller compared to some earlier studies.[6,8] This may result from the smaller number of subregions in the multiblock model, different vessel size, or varying agitation conditions in the present simulation case. Another reason could be the assumption of constant bubble size in earlier studies. Tiny bubbles (<1 mm) predicted by the population balance model have low slip velocities and they are transported to the quiescent zones of the reactor even at low liquid flow rates. In the present model, small bubbles are assumed to be effective for the mass transfer as a result of the continuous breakage-coalescence process. This seems to explain the rather smooth variation of DO in the fermenter.

The spatial distribution of the xanthan reaction rate is very similar to the DO (Figure 14). Reaction rates are largest at the

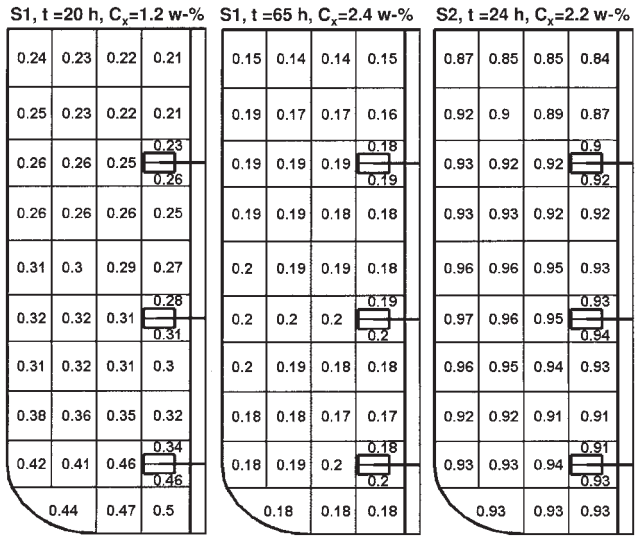

Figure 14. Predicted distribution of xanthan reaction rates (r_X, gX/L/h) in the 0.64 m^3 fermenter.

bottom of the reactor and in the impeller discharge flows. High reaction rates near the wall seem to result from the convection of the DO with the impeller discharge flow and the transfer of oxygen from tiny bubbles. Xanthan reaction rates decrease most clearly in the quiescent zones of the reactor towards the end of fermentation (S1, t = 65 h).

Conclusions

A dynamic multiblock model was created for the agitated xanthan fermenter and laboratory stirred tank. The change of flow fields was related to the xanthan concentration based on CFD simulations. Local gas-liquid mass transfer areas were modeled with adaptively discretized population balances for bubbles. Gas-liquid mass transfer fluxes were obtained from the simplified solution of Maxwell-Stefan multicomponent diffusion by assuming mass transfer resistances in both the gas and liquid side. The reactor model is computationally efficient, allowing the simulation of a whole fermentation batch, which is not possible with CFD at present computational capabilities.

The population balance and gas-liquid mass transfer models were validated against hydrodynamic and oxygen transfer experiments from aqueous xanthan solutions in a laboratory stirred tank. The results show that local bubble size distributions (BSD) are needed to describe complex gas-liquid hydrodynamics and mass transfer accurately in a highly viscous, non-Newtonian dispersion. In view of the complexity of the investigated system, the agreement between the simulations and experiments is good.

Dynamic simulations of a pilot fermenter revealed the change of mixture homogeneity during the fermentation batch. The results agree with the experimental studies of xanthan fermentation and indicate that oxygen transfer and poor mixing are bottlenecks in this process. It seems that modeling uncertainties of one phenomenon do not affect the overall predictions much, because several phenomena, such as mixing and mass transfer, limit the reactor performance simultaneously. The model predicts the effect of operating conditions on the temporal and spatial variation of BSDs, mass transfer coefficients, dissolved oxygen concentrations, and xanthan reaction rates in the fermenter. It can be used to investigate fermenter operating strategies. The model is also useful for the scale-up studies.

Acknowledgments

The authors want to thank B.Sc. Asta Nurmela, M.Sc. Suvi Jussila, and Ms. Elina Nauha for carrying out the experiments. Financial support from the Graduate School of Chemical Engineering, and the Neobio (New design tool for bioreactors) and ModCheR (Modelling of Chemical Reactors) projects funded by the National Technology Agency of Finland (Tekes) is acknowledged.

Notation

$\hat{z}$ = *unit vector in axial direction*
a_L = specific mass transfer area, m^2/m^3(liquid)
#($V_p/2$) = index number of size category of characteristic volume $V_p/2$
a,b,e = adjustable parameters in the multiblock model
A_k = the surface area of bubble, m^2
A_h = area of the bubble projection on the orthogonal plane of bubble flow, m^2
A_{ij} = area over which the liquid flows from subregion i to j, m^2
$b(d_k)$ = bubble growth due to mass transfer, 1/s
$B(d_k)$ = volumetric bubble growth rate due to mass transfer, m^3/s
c_{O2}, c_{CO2} = concentration, mol/L
c_B, c_X, c_S, c_N = concentration, g/L
c_{ij} = binary connectivity between subregions i and j (= 1 if connected, =0 otherwise)
C_1-C_5 = adjustable model parameters
C_D = bubble drag coefficient
d = bubble diameter, m
d_{10} = arithmetic mean bubble diameter ($=\Sigma d_i/\Sigma i$), m
d_{32} = Sauter mean bubble diameter ($=\Sigma d_i^3/\Sigma d_i^2$), m
D_L = liquid phase diffusion coefficient, m^2/s
D_I = impeller diameter, m
DO = dissolved oxygen
DCO = dissolved carbon dioxide
E(d) = aspect ratio of bubble
F_{ij} = liquid flow rate from subregion i to j, m^3/s
F^*_{ij} = impeller speed independent liquid flow rate ($= F_{ij}/N{\cdot}D_I^3$)
f = breakage volume fraction
g = acceleration due to gravity (= 9.81 m/s^2)
$g(d_p)$ = breakage frequency, 1/s
GR = Geary's ratio, dimensionless
H = vessel height, m
He = Henry's constant, Pa
$h(a_k,a_p)$ = coalescence frequency, m^3/s
h = solubility parameter, L/mol
K = consistency index in power law viscosity model, $kg{\cdot}s^{n-2}/m$
k_L = mass transfer coefficient in the liquid film, m/s
k_La = overall mass transfer coefficient, 1/s
Mo = Morton number ($g{\cdot}\mu_{eff}^4 / (\rho_C{\cdot}\sigma^3)$)
N = stirring speed, 1/s
n = flow index
NB = number of multiblock model subregions
NC = number of chemical compounds
NI = number of ionic species
N_m = mass transfer flux, $mol/m^2/s$
NP = number of bubble size categories
N_p = power number ($P/(\rho_C{\cdot}D_I^5N^3)$)
NS = number of scalars
OTR = oxygen transfer rate, mmol/L/h
P = mixing power, $kg{\cdot}m^2/s^3$
Q = gassing rate, m^3/s
r_{O2}, r_{CO2} = reaction rate, mol/L/h
r_B, r_X, r_S, r_N = reaction rate, g/L/h
Re = bubble Reynolds number ($= d{\cdot}U_{slip}\rho_C/\mu_{eff}$)
Re_I = impeller Reynolds number ($= D_I^2{\cdot}N{\cdot}\rho_C/\mu_{eff}$)
s = variable
SD = relative standard deviation, dimensionless
T = vessel diameter, m
t = time, s
U = bubble velocity, m/s
v = bubble volume, m^3
V_i = volume of a subregion, m^3
V_S = superficial gas velocity, m/s
V_T = vessel volume, m^3
$\bar{V}_m$ = partial molar volume of component, m^3/mol
vvm = m^3(gas)/m^3(liquid)/min
We = Weber number ($= \rho_C{\cdot}d^{5/3}{\cdot}\varepsilon^{2/3}/\sigma$)
x = component mole fraction in liquid phase
y = component mole fraction in gas phase
Y_k = number bubbles k per unit volume, $1/m^3$

Greek letters

$\beta(d_k,d_p)$ = probability that a bubble of size d_k is formed when d_p breaks, 1/m
γ = shear rate, 1/s
Δd = the width of bubble size category, m
ε = dissipation rate of turbulent energy, m^2/s^3
ϕ = gas volume fraction
μ_∞ = apparent viscosity at infinite shear, kg/m/s

μ_0 = apparent viscosity at zero shear, kg/m/s
μ_{eff} = apparent, local liquid viscosity, kg/m/s
λ = viscosity model parameter, s
$\lambda(d_k,d_p)$ = coalescence efficiency
λ_d = size of turbulent eddy, m
∇p = dynamic pressure gradient, kg/m^2/s^2
ξ = ratio of minimum eddy size and bubble size
σ = surface tension, kg/s^2
θ = temperature, °C
ρ_D, ρ_C = density of dispersed and continuous phase, kg/m^3
τ = relaxation parameter of the extra volume in a subregion. s

Subscripts

0 = initial concentration or volume
B = biomass, bulk composition
CO2 = carbon dioxide
g = gassed
G = gas phase
I = composition at gas-liquid interface
i, j, n = index of multiblock model subregion
k, p = index of bubble size category
L = liquid phase
m = index of chemical compound
min = minimum
mix = fermentation mixture
N = nutrient
O2 = oxygen
S = carbon source
t = total concentration
u = ungassed
X = xanthan

Literature Cited

1. Schügerl K, Bellgardt KH. *Bioreaction Engineering, Modeling and Control*. Berlin: Springer Verlag; 2000.
2. Gogate PR, Beenackers AACM, Pandit A. Multiple-impeller systems with a special emphasis on bioreactors: a critical review. *Biochem Eng J.* 2000;6:109-143.
3. Mann R, Hackett LA. Fundamentals of gas-liquid mixing in a stirred vessel: an analysis of networks of backmixed models. In: Proceedings of 6th European Conference on Mixing, Pavia, Italy, 24-26th May, BHRA, 1988:321-328.
4. Vasconcelos JMT, Alves SS, Barata JM. Mixing in gas-liquid contactors agitated by multiple turbines. *Chem Eng Sci.* 1995;50:2343-2354.
5. Vrábel P, van der Lans RGJM, Luyben KCAM, Boon L, Nienow AW. Mixing in large-scale vessels stirred with multiple radial or radial and axial up-pumping impellers: modelling and measurements. *Chem Eng Sci.* 2000;55:5881-5896.
6. Vlaev D, Mann R, Lossev V, Vlaev SD, Zahradnik J, Seichter P. Macro-mixing and streptomyces fradiae—modelling oxygen and nutrient segregation in an industrial bioreactor. *Chem Eng Research Design.* 2000;78A:354-362.
7. Zahradnik J, Mann R, Fialova M, Vlaev D, Vlaev SD, Lossev V, Seichter P. A network-of-zones analysis of mixing and mass transfer in three industrial bioreactors. *Chem Eng Sci.* 2001;56:485-492.
8. Hristov H, Mann R, Lossev V, Vlaev SD, Seichter P. A 3-D analysis of gas-liquid mixing, mass transfer and bioreaction in a stirred bioreactor. *Chem Eng Research Design.* 2001;79C:232-241.
9. Alopaeus V, Koskinen J, Keskinen KI, Majander J. Simulation of the population balances for liquid-liquid systems in a nonideal stirred tank. Part 2—parameter fitting and the use of the multiblock model for dense dispersions. *Chem Eng Sci.* 2002;57:1815-1825.
10. Laakkonen M, Alopaeus V, Aittamaa J. Validation of bubble breakage, coalescence and mass transfer models for gas-liquid dispersion in agitated vessels. *Chem Eng Sci.* 2006;61:218-228.
11. Zauner R, Jones AG. On the influence of mixing on crystal precipitation processes—application of the segregated feed model. *Chem Eng Sci.* 2002;57:821-831.
12. Bezzo F, Macchietto S, Pantelides CC. General hybrid multizonal/CFD approach for bioreactor modeling. *AIChE J.* 2003;49:2133-2148.
13. Bezzo F, Macchietto S, Pantelides CC. A general methodology for hybrid multizonal/CFD models Part I. Theoretical framework. *Computers Chem Eng.* 2004;28:501-511.
14. Wells GJ, Ray WH. Methodology for modeling detailed imperfect mixing effects in complex reactors. *AIChE J.* 2005;51:1508-1520.
15. Galindo E. Aspects of the process for xanthan production. *Chem Eng Research Design.* 1994;72C:227-237.
16. Amanullah A, Serrano-Carreon L, Castro B, Galindo E, Nienow AW. The influence of impeller type and pilot scale xanthan fermentations. *Biotech Bioeng.* 1998;51:95-108.
17. Garcia-Ochoa F, Gomez-Castro E, Santos VE. Oxygen transfer and uptake rates during xanthan gum production. *Enzyme Microbial Tech.* 2000;27:680-690.
18. Amanullah A, Tuttiett B, Nienow AW. Agitator speed and dissolved oxygen effects in xanthan fermentations. *Biotech Bioeng.* 1998;57:198-210.
19. Serrano-Carreón L, Corona RM, Sánchez A, Galindo E. Prediction of xanthan fermentation development by a model linking kinetics, power drawn and mixing. *Process Biochem.* 1998;33:133-146.
20. Flores F, Torres LG, Galindo E. Effect of the dissolved oxygen tension during cultivation of X. Campestris on the production and quality of xanthan gum. *J Biotech.* 1994;34:165-173.
21. van't Riet K. Review of measuring methods and results in nonviscous gas-liquid mass transfer in stirred vessels. *Industrial Chem Process Design Development.* 1979;18:357-364.
22. Garcia-Ochoa F, Santos VE, Alcón A. Xanthan gum production: an unstructured kinetic model. *Enzyme Microbial Tech.* 1995;17:206-217.
23. Letisse F, Lindley ND, Roux G. Development of a phenomenological modeling approach for prediction of growth and xanthan gum production using *Xanthomonas campestris. Biotech Progress.* 2003;19:822-827.
24. Garcia-Ochoa F, Santos VE, Alcón A. Metabolic structured kinetic model for xanthan production. *Enzyme Microbial Tech.* 1998;23:75-82.
25. Seáñez G, Peña C, Galindo E. High CO_2 affects alginate production and prevents polymer degradation in cultures of *Azotobacter vinelandii. Enzyme Microbial Tech.* 2001;29:535-540.
26. Carreau PJ. Rheological equations from molecular network theories. *Transactions Soc Rheology.* 1972;16:99-127.
27. Moilanen P, Laakkonen M, Aittamaa J. Modelling fermenters with CFD. In: Proceedings of the 15th European Symposium on Computer Aided Process Engineering, May 29-June 1, 2005, Barcelona, Spain.
28. Alopaeus V, Koskinen J, Keskinen K. Simulation of the population balances for liquid-liquid systems in a nonideal stirred tank. Part 1: Description and qualitative validation of the model. *Chem Eng Sci.* 1999;54:5887-5899.
29. Gray JB. *Mixing—Theory and Practice*. New York: Academic Press, 1966: vol 1, Chap 4:180-184.
30. Bakker A, van den Akker HEA. A computational model for the gas-liquid flow in stirred reactors. *Chem Eng Research Design.* 1994;72A:594-606.
31. Elson TP, Cheesman DJ, Nienow AW. X-ray studies of cavern sizes and mixing performance with fluids possessing a yield stress. *Chem Eng Sci.* 1986;41:2555-2562.
32. Khare AS, Niranjan K. Impeller-agitated aerobic reactor: the influence of tiny bubbles on gas hold-up and mass transfer in highly viscous liquids. *Chem Eng Sci.* 1995;50:1091-1105.
33. Venneker BCH, Derksen JJ, van den Akker HEA. Population balance modelling of aerated stirred vessels based on CFD. *AIChE J.* 2002;48:673-685.
34. Hulburt HM, Katz S. Some problems in particle technology. *Chem Eng Sci.* 1964;19:555-574.
35. Valentas KJ, Amundson NR. Breakage and coalescence in dispersed phase systems. *Industrial Eng Chem Fundamentals.* 1966;5:533-542.
36. Ramkrishna D. *Population Balances: Theory and Applications to Particulate Systems in Engineering*. San Diego: Academic Press; 2000.
37. Tzounakos A, Karamanev DG, Margaritis A, Bergougnou MA. Effect of the surfactant concentration on the rise of gas bubbles in power-law non-Newtonian liquids. *Industrial Eng Chem Research.* 2004;43:5790-5795.
38. Miyahara T, Yamanaka S. Mechanics of motion and deformation of a single bubble rising through quiescent highly viscous Newtonian and non-Newtonian media. *J Chem Eng Japan.* 1993;26:297-302.
39. Jakobsen HA, Lindborg H, Dorao C. Modeling of bubble column

reactors: progress and limitations. *Industrial Eng Chem Research.* 2005;44:5107-5151.
40. Luo H, Svendsen HF. Theoretical model for drop and bubble breakup in turbulent dispersions. *AIChE J.* 1996;42:1225-1233.
41. Hagesaether L, Jakobsen HA, Svendsen HF. A model for turbulent binary breakup of dispersed fluid particles. *Chem Eng Sci.* 2002;57: 3251-3267.
42. Lehr F, Millies M, Mewes D. Bubble-size distributions and flow fields in bubble columns. *AIChE J.* 2002;48:2426-2443.
43. Wang T, Wang J, Jin Y. A novel theoretical breakup kernel function for bubbles/droplets in a turbulent flow. *Chem Eng Sci.* 2003;58:4629-4637.
44. Hesketh RP, Etchells AW, Russell TWF. Bubble breakage in pipeline flow. *Chem Eng Sci.* 1991;46:1-9.
45. Coulaloglou CA, Tavlarides LL. Description of interaction processes in agitated liquid-liquid dispersions. *Chem Eng Sci.* 1977;32:1289-1297.
46. Chaudhari RV, Hofmann H. Coalescence of gas bubbles in liquids. *Reviews in Chem Eng.* 1994;10:131-190.
47. Chesters KA. The modelling of coalescence processes in fluid-liquid dispersions: a review of current understanding. *Chem Eng Research Design.* 1991;69:259-270.
48. Prince MJ, Blanch HW. Bubble coalescence and break-up in air-sparged bubble columns. *AIChE J.* 1990;36:1485-1499.
49. Luo H. Thesis, Trondheim, Department of Chemical Engineering, The Norwegian Institute of Technology, 1993.
50. Laakkonen M, Moilanen P, Miettinen T, Saari K, Honkanen M, Saarenrinne P, Aittamaa J. Local bubble size distributions in agitated vessels—comparison of three experimental techniques. *Chem Eng Research Design.* 2005;83A:50-58.
51. Taylor R, Krishna R. *Multicomponent Mass Transfer*. New York: Wiley & Sons, Inc.; 1993.
52. Alopaeus V. Ph.D. Thesis, Helsinki University of Technology, 2001. http://lib.tkk.fi/Diss/2001/isbn9512257041/.
53. Higbie R. The rate of absorption of a pure gas into a still liquid during short periods of exposure. *Transactions American Institution of Chem Engineers.* 1938;35:360-365.
54. Frössling N. On the evaporation of falling droplets. *Gerlands Beitage Geophysik.* 1938;52:170-216.
55. Kawase Y, Halard B, Moo-Young M. Liquid phase mass transfer coefficients in bioreactors. *Biotech Bioeng.* 1992;39:1133-1140.
56. Garcia-Ochoa F, Gomez E. Theoretical prediction of gas-liquid mass transfer coefficient, specific area and hold-up in sparged stirred tanks. *Chem Eng Sci.* 2004;59:2489-2501.
57. Alopaeus V. Mass-transfer calculation methods for transient diffusion within particles. *AIChE J.* 2000;46:2369-2372.
58. Weissenberger S, Schumpe A. Estimation of gas solubilities in salt solutions at temperatures from 273 K to 363 K. *AIChE J.* 1996;42: 298-300.
59. Rischbieter E, Schumpe A. Gas solubilities in aqueous solutions of organic substances. *J Chem Eng Data.* 1996;41:809-812.
60. Fogg PGT, Gerrard W. *Solubility of Gases in Liquids: A Critical Evaluation of Gas/Liquid Systems in Theory and Practice*. New York: John Wiley and Sons; 1991.
61. Tatterson GB. *Fluid Mixing and Gas Dispersion in Agitated Tanks*. New York: McGraw-Hill; 1991.
62. Vlaev SD, Valeva MD, Mann R. Some effects of rheology on the spatial distribution of gas holdup in a mechanically agitated vessel. *Chem Eng J.* 2002;87:21-30.
63. Nienow AW, Hunt G, Buckland BC. A fluid dynamic study using a simulated viscous, shear thinning broth of the retrofitting of large agitated bioreactors. *Biotech Bioeng.* 1996;49:15-19.
64. Cui YQ, van der Lans RGJM, Luyben KChAM. Local power uptake in gas-liquid systems with single and multiple Rushton turbines. *Chem Eng Sci.* 1996;51:2631-2636.
65. Philip J, Proctor JM, Niranjan K, Davidson JF. Gas holdup and liquid circulation in internal loop reactors containing highly viscous Newtonian and non-Newtonian liquids. *Chem Eng Sci.* 1990;45:651-664.
66. Wilke CR, Chang P. Correlation of diffusion coefficients in dilute solutions. *AIChE J.* 1955;1:264-270.
67. Poling BE, Prausnitz JM, O'Connell JP. *The Properties of Gases and Liquids*. New York: McGraw-Hill; 2000.
68. Metzner AB, Otto RE. Agitation of non-Newtonian fluids. *AIChE J.* 1957;1:3.
69. Jackson ML, Shen C-C. Aeration and mixing in deep tank fermentation systems. *AIChE J*. 1978;24:63-71.
70. Machon VV, Vlcek J, Nienow AW, Solomon J. Some effects of pseudoplasticity on hold-up in aerated, agitated vessels. *Canadian J Chem Eng.* 1980;19:67.
71. Peters HU, Herbst H, Hesselink PGM, Lünsdorf H, Schumpe A, Deckwer WD. The influence of agitation rate on xanthan production by Xanthomonas campestris. *Biotech Bioeng.* 1989;34:1393-1397.

Manuscript received July 28, 2005, revision received Oct. 31, 2005, and final revision received Jan. 2, 2006.